Opto-Electronic Science

Ppt-level volatile organic compounds detection via microsecond-pulse-enhanced mid-infrared photoacoustic

Senyu Wang†, Liang Zhao†, Hongyu Luo†, Xiangyu Zhao, Jianfeng Li*, Wei Wang, Hao Lei, Mingrui Jiang, Jinlong Wan, Binxing Zhao, Bincheng Li and Yong Liu

https://doi.org/10.29026/oes.2026.260008

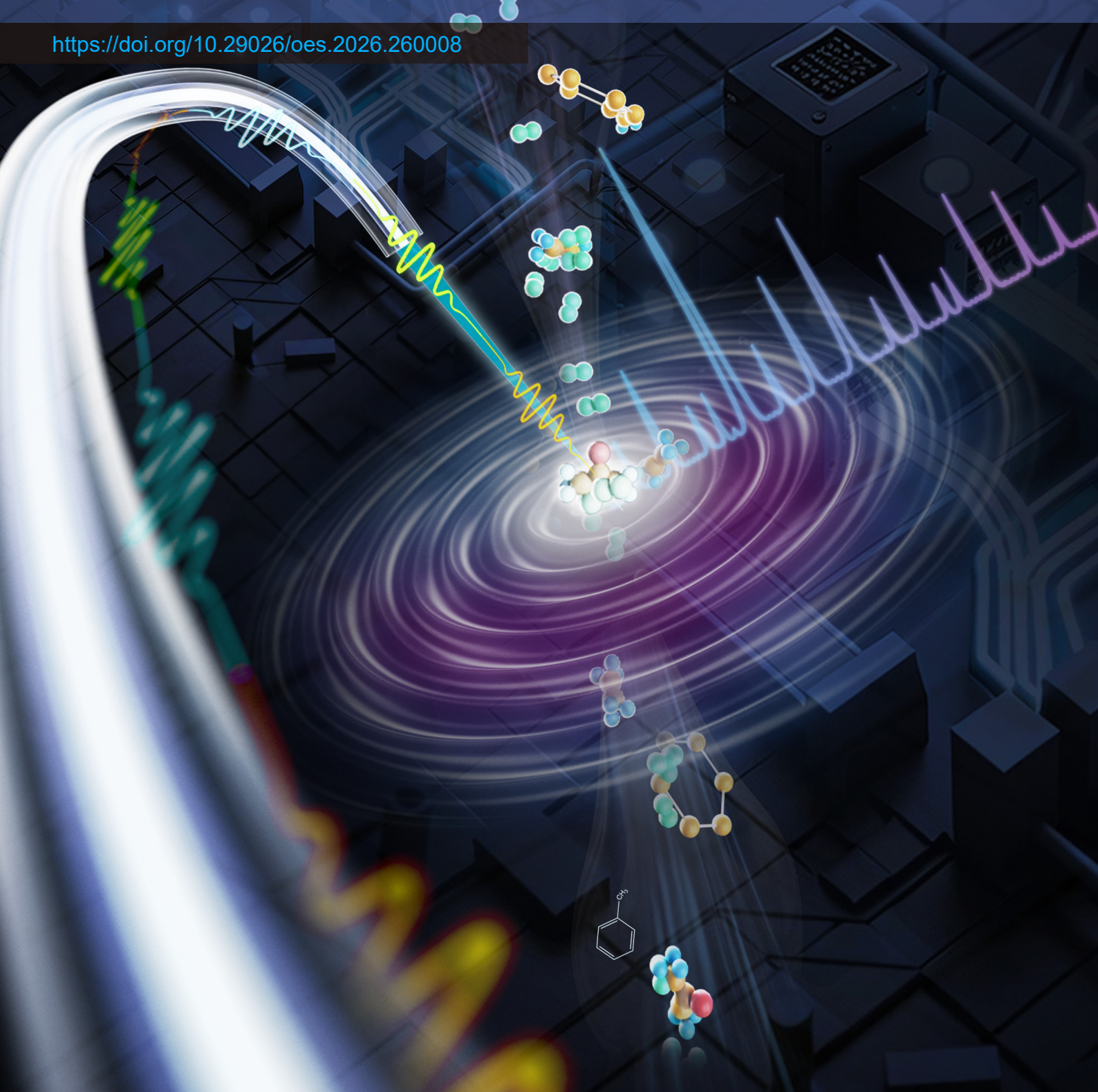

Opto-Electronic Science

CN 51-1800/O4 ISSN (Print) 2097-0382 ISSN (Online) 2097-4000

Ppt-level volatile organic compounds detection via microsecond-pulse-enhanced mid-infrared photoacoustic

Senyu Wang, Liang Zhao, Hongyu Luo, Xiangyu Zhao, Jianfeng Li*, Wei Wang, Hao Lei, Mingrui Jiang, Jinlong Wan, Binxing Zhao, Bincheng Li and Yong Liu

Citation: Wang SY, Zhao L, Luo HY et al. Ppt-level volatile organic compounds detection via microsecond-pulse-enhanced mid-infrared photoacoustic. *Opto-Electron Sci* **5**, 260008 (2026).

https://doi.org/10.29026/oes.2026.260008

Received: 5 February 2026; Accepted: 6 March 2026; Published online: 30 March 2026

OES | Opto-Electronic Science

Article

April 2026, Vol. 5, No. 4

Open Access

Ppt-level volatile organic compounds detection via microsecond-pulse-enhanced mid-infrared photoacoustic

Senyu Wang[1,3†], Liang Zhao[1†], Hongyu Luo[1†], Xiangyu Zhao[1], Jianfeng Li[1,2*], Wei Wang[1], Hao Lei[1], Mingrui Jiang[1], Jinlong Wan[1], Binxing Zhao[1], Bincheng Li[1] and Yong Liu[1]

Abstract: Ultrasensitive detection of volatile organic compounds (VOCs) is pivotal for early disease diagnosis and industrial safety, yet existing photoacoustic spectroscopy (PAS) systems struggle to breach the sub-ppb barrier required for practical applications. Here, we overcome this limitation by demonstrating a PAS architecture driven by a gain-switched Er^{3+}/Dy^{3+} co-doped mid-infrared fiber laser, achieving an unprecedented detection limit of 416 ppt for propane, which is an order-of-magnitude improvement over state-of-the-art systems. This performance arises from a direct pump-modulation strategy that generates high-energy microsecond pulses to significantly enhance photoacoustic excitation without power loss. Crucially, the laser's broad tunability (3.2–3.55 μm) covers the fundamental C-H stretching band, enabling not only high-resolution spectral reconstruction but also the versatile detection of multiple disease markers and industrial hazards, including isoprene (cardiovascular biomarker), 1,2-dimethoxyethane (battery failure indicator), and propanal (food safety marker). By delivering clinical-grade sensitivity in a compact, robust fiber-based format, this work establishes a transformative pathway toward deployable, high-performance gas sensing solutions.

Keywords: photoacoustic spectroscopy; mid-infrared fiber laser; volatile organic compounds; trace gas detection

DOI: 10.29026/oes.2026.260008 | CSTR: 32246.14.oes.2026.260008

Citation: Wang SY, Zhao L, Luo HY et al. Ppt-level volatile organic compounds detection via microsecond-pulse-enhanced mid-infrared photoacoustic. *Opto-Electron Sci* **5**, 260008 (2026).

1 Introduction

Trace-level detection of volatile organic compounds (VOCs) at parts-per-billion (ppb) to parts-per-trillion (ppt) concentrations has become increasingly critical for environmental monitoring, medical diagnostics, and industrial safety. In medical applications, specific VOCs in exhaled breath serve as biomarkers for lung cancer, diabetes, and other diseases, requiring detection sensitivities below few-ppb levels for early diagnosis[1,2]. Environmental regulations increasingly demand real-time monitoring of hazardous VOCs such as benzene, formaldehyde, and toluene at stringent exposure limits[3,4]. These applications demand detection technologies that combine extreme sensitivity, high selectivity, rapid response, and operational simplicity, yet current analytical methods cannot simultaneously satisfy all these requirements. While gas chromatography-mass spectrometry (GC-MS) provides excellent selectivity, it lacks real-time capability; optical methods like cavity ring-down spectroscopy and dual-comb spectroscopy achieve high sensitivity but require complex setups; and chemical sensors offer portability at the expense of selectivity[5–9]. Recently, photoacoustic (PA) spectroscopy emerges as the most promising solution, converting optical absorption directly into acoustic signals with remarkable sensitivity through resonance enhancement while maintaining system simplicity[10–17].

The transformative potential of PA spectroscopy for VOC detection remains constrained by limitations in available laser technologies and modulation strategies. From the laser perspective, the 3.2–3.5 μm spectral region (containing fundamental C–H stretching vibrations present in virtually all organic compounds) represents the optimal window for

Received: 5 February 2026

Accepted: 6 March 2026

Published online: 30 March 2026

[1]School of Optoelectronic Science and Engineering, University of Electronic Science and Technology of China, Chengdu 610054, China; [2]Tianfu Jiangxi Laboratory, Chengdu 641419, China; [3]Institute for Photon Science and Technology, School of Science, The University of Tokyo, Tokyo 113-0033, Japan.

[†]These authors contributed equally to this work.

*Correspondence: JF Li, E-mail: lijianfeng@uestc.edu.cn

VOC detection due to absorption cross-sections exceeding 10^{-19} cm^2/molecule (detailed shown in Supplementary Section 1). However, existing laser sources face critical limitations in this band: quantum cascade lasers (QCL), the most widely used mid-infrared (MIR) lasers, cannot access this spectral region; interband cascade lasers (ICL) deliver insufficient power (<50 mW) for trace gas detection; and optical parametric oscillators (OPO) suffer from complexity and instability[18–23]. While MIR fiber lasers promise high power, broad tunability, and excellent stability, existing implementations using gas-filled hollow-core fiber laser or fiber supercontinuum sources remain proof-of-concept demonstrations without significant performance improvements[24–27]. Remarkably, rare-earth-doped MIR fiber lasers (the most mature and practical MIR fiber laser technology) have never been explored for PA gas sensing despite their compelling advantages[28,29]. From the modulation perspective, the broad absorption spectra of large-molecule VOCs make conventional wavelength modulation spectroscopy with 2*f* (WMS-2*f*) demodulation ineffective[10,11]. Intensity modulation approaches using mechanical choppers or acousto-optic modulators (AOM) sacrifice over 50% of optical power while introducing mechanical noise, severely limiting the achievable detection sensitivity for trace VOC analysis[30,31]. Consequently, the field of PA VOC sensing confronts a compounded bottleneck: the scarcity of high-power, stable sources in the critical 3.2–3.5 μm window, exacerbated by the inefficiency of traditional modulation schemes that introduce excessive loss and noise. Overcoming these intertwined limitations necessitates a novel system architecture capable of bridging high-power generation with efficient excitation.

Here, we report the first PA VOC detection system based on rare-earth-doped MIR fiber laser, introducing microsecond-pulse-enhanced photoacoustic spectroscopy (MPEPAS) that fundamentally overcomes existing limitations. Through theoretical analysis and experimental validation, we discovered that microsecond pulses at kHz repetition rates achieve optimal coupling with acoustic resonator frequencies, enhancing PA signals without power loss. We pioneered gain-switched (GS) operation in an Er^{3+}/Dy^{3+} co-doped fiber laser system, generating 2.3 μs pulses with 245 mW output power and broadband tunability across the entire C-H fingerprint region (3200–3550 nm). This approach delivers two-fold signal enhancement compared to conventional continuous-wave modulation under identical injection power. The system achieved a record-breaking propane detection limit of 416 ppt with 200 s averaging, surpassing previous PA detection limits by over an order of magnitude. Leveraging the laser's broadband tunability, we reconstructed propane's absorption spectrum with <0.8 nm resolution. The system also achieved detection limits of 1.8 ppb for propanal, 2.67 ppb for isoprene, and 850 ppt for 1,2-dimethoxyethane, representing different VOC categories including aldehydes, alkenes, and ethers. This breakthrough establishes a new paradigm for ultra-sensitive VOC sensing with immediate applications in environmental monitoring, precision medicine, and smart manufacturing. The combination of extreme sensitivity, broad spectral coverage, and inherent system simplicity enables previously impossible applications, from early cancer detection through breath analysis to real-time monitoring of industrial emissions at regulatory limits.

2 Results

2.1 Mechanism of MPEPAS

Modulated resonant PA is a sensitive technique for trace gas sensing and has been well established. Generally, a continuous wave (CW) laser is modulated using an AOM or a chopper at the resonant frequency of an acoustic resonator to exploit the standing wave superposition effect of the acoustic field for PA response enhancement. Typically, a duty cycle of approximately 50% is employed to maximize the PA effect. Indeed, around 50% represents the optimal duty cycle parameter for maximum PA signal strength, but this does not necessarily mean that 50% duty cycle modulated pulses possess the highest PA excitation efficiency. Here, we define a metric: PA excitation efficiency η, where $\eta=S/P$, with S being the lock-in detected PA response and P being the average laser power. Therefore, η has units of V/W. Bartlome R et al. have demonstrated that picosecond to nanosecond excitation can effectively enhance PA response efficiency[32]. However, for modulation methods based on choppers or AOMs, reducing the time duration results in a dramatic decrease in power. Consequently, although PA excitation efficiency improves, the PA signal is significantly reduced. Therefore, an alternative operational mode—pulsed resonant PA—has emerged, which employs a pulsed laser to match the acoustic resonance, leveraging the high PA excitation efficiency of pulsed lasers to achieve enhanced PAS. Bartlome R et al. have discussed the pulsed case where $\tau_p \ll \tau_{VT}$, namely, pulse duration much shorter than vibrational-translational process, i.e., the scenario of nanosecond and picosecond pulses[32]. Here, we investigate submicrosecond and microsecond pulses on the same timescale as τ_{VT}, a regime that is most promising for PA gas detection, as their kHz-level repetition rates match the typical frequencies of acoustic resonators while simultaneously delivering high pulse energy for strong PA excitation.

Figure 1(a) illustrates the vibration and thermal behaviors in the PA excitation, showing the complete energy conversion process from molecular vibration to thermal equilibrium. When MIR laser radiation is absorbed by target bonds in the gas molecules, specific vibrational modes are excited from the ground state (v_0) to higher vibrational levels (v_1). During the subsequent non-radiative relaxation phase, the excited molecules undergo vibrational-translational energy transfer through intermolecular collisions with

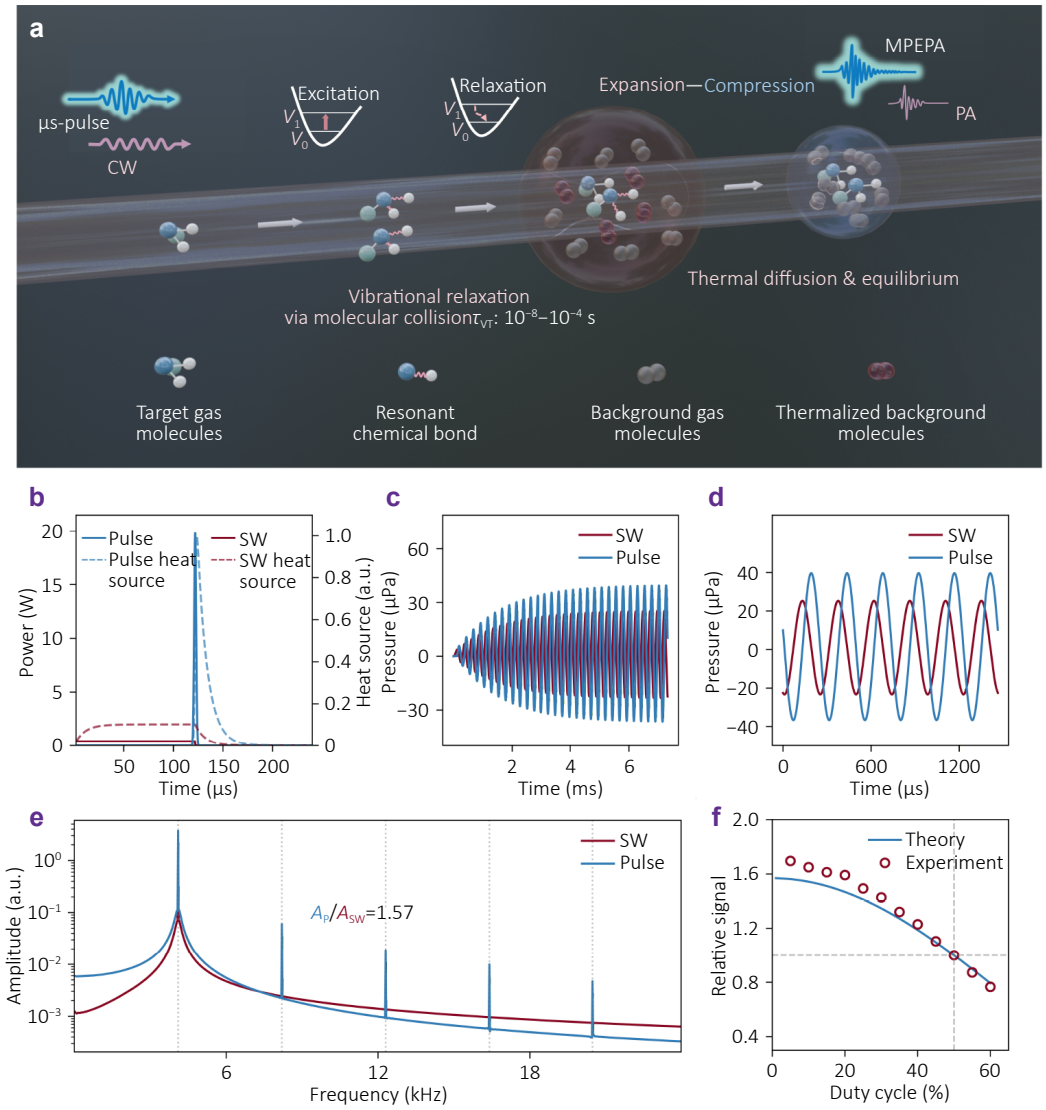

Fig. 1 | Schematic and comparison of PA responses from microsecond pulse laser and modulated square wave laser excitation. (a) Schematic of the molecular-level PA process, encompassing vibrational excitation, non-radiative relaxation, and thermal diffusion. (b) Simulated temporal profiles of pulse and modulated CW laser and the corresponding heat source. SW; modulated square wave. (c) Transient acoustic pressure response of the first-order longitudinal mode in the resonant PA cell for both excitation methods. (d) A detailed view of the steady-state response of (c). (e) Fourier transform of the steady-state signals, quantifying that the fundamental frequency amplitude of the low duty-cycle pulsed response is 1.57 times that of the modulated square wave. (f) Theoretical and experimental PA excitation efficiency at various modulation duty cycles, normalized to the signal at 50%.

background gas molecules (primarily nitrogen), converting vibrational energy into translational kinetic energy. This process generates localized heating within the gas mixture, inducing gas expansion and consequently producing acoustic pressure. Finally, thermal diffusion and equilibrium processes redistribute the heat throughout the system, restoring the initial conditions before the arrival of the next pulse.

In CW-modulated PA, the laser intensity follows a square wave profile with extended pulse duration. The resulting heat generation exhibits a broad temporal distribution spanning both the vibrational excitation/non-radiative relaxation. In contrast, the high peak power low duty-cycle pulsed (LDCP) excitation, which concentrates the energy deposition within a narrow time window, resulting in more efficient PA signal generation due to the enhanced thermal confinement and reduced heat diffusion losses during the excitation phase. These two distinct thermal-temporal behaviors result in a strong pulse-duration dependence of the PA response. To simulate the PA signal generation in gas-phase media, we adopt a two-level energy model to describe the light-induced excitation and subsequent vibration relaxation processes[33]. The two-level system under weak absorption conditions can be written as:

$$\frac{\mathrm{d}N_1}{\mathrm{d}t} = N_0\sigma\Phi(r,\ t) - \frac{N_1(r,\ t)}{\tau_{\mathrm{VT}}}\ , \tag{1}$$

where N_0 and N_1 are the ground and excited state population densities, respectively, τ_{VT} is the vibrational-translational relaxation time. $\Phi(t)$ is the photon flux, which is calculated from the laser power profile as:

$$\Phi(r,t) = \frac{P(t)}{h\nu\pi r_{\mathrm{b}}^2}\ , \tag{2}$$

where $P(t)$ describes the temporal modulation of the laser intensity (e.g., square wave or pulse), h is Planck's constant, ν is the optical frequency, and r_{b} is the beam radius. Here, the uniform beam approximation was employed. This simplification is justified since the beam radius (0.4 mm) is significantly small compared to the resonator radius (2.5 mm), rendering the acoustic excitation insensitive to the specific transverse beam profile. The volumetric heat source, representing the thermal energy released due to non-radiative relaxation, is directly proportional to the decay rate of the excited state population:

$$H(r,t) = \frac{h\nu N_1(r,t)}{t\tau_{\mathrm{VT}}}\ . \tag{3}$$

The periodic heat source, $H(r,\ t)$, induces periodic changes in the local pressure, temperature, and density of the gas, thereby generating an acoustic wave. In a cylindrical resonator, the behavior of the acoustic pressure wave, $p(z,\ t)$, can be described by the inhomogeneous Helmholtz equation[34]. For a specific acoustic mode (the first longitudinal mode in this study), the temporal evolution of its pressure amplitude, $A(t)$, follows a forced damped harmonic oscillator model of:

$$\frac{\mathrm{d}^2A}{\mathrm{d}t^2} + 2\xi\omega_1\frac{\mathrm{d}A}{\mathrm{d}t} + \omega_1^2A = F(t)\ , \tag{4}$$

where $\omega_1=2\pi f_1$, f_1 is the resonant frequency of the first longitudinal mode, $\xi = 1/(2Q)$ is the damping ratio of the PA cell, and the modal driving force is:

$$F(t) = \beta H(t) S_{\mathrm{overlap}}\ , \tag{5}$$

where β and S_{overlap} is the thermoacoustic coefficient and the spatial overlap factor, respectively. Exploiting the periodic nature of the excitation and assuming complete relaxation between pulses ($\tau_{\mathrm{VT}} \ll T/2$), we solve the two-level dynamics for a single modulation period with periodic boundary conditions. For the special case of extremely short relaxation times (τ_{VT} <50 ns), where the relaxation timescale is orders of magnitude shorter than the optical excitation envelope, the system response is considered instantaneous. Consequently, the program adopts a quasi-steady-state approximation (adiabatic following), assuming the population density implicitly tracks the laser intensity profile, which is expressed as:

$$N_1^{\mathrm{QSS}}(t) = N_0\sigma\Phi(t)\tau_{\mathrm{VT}}\ . \tag{6}$$

The modal amplitude is computed through time-domain convolution with the Green's function:

$$A(t) = \int_0^t F(\tau)G(t-\tau)\mathrm{d}\tau\ , \tag{7}$$

where the Green's function for the damped harmonic oscillator is:

$$G(t) = \frac{1}{\omega_{\mathrm{d}}}\exp(-\xi\omega_1 t)\sin(\omega_{\mathrm{d}}t)\ , \tag{8}$$

with $\omega_{\mathrm{d}}=\omega_1\sqrt{1-\xi^2}$. The frequency spectrum is computed using FFT on 200 periods of the steady-state signal. While specific τ_{VT} relaxation times for propane in a nitrogen matrix are not well-documented, the self-relaxation time of propane was known to be approximately 15.6 ns[35]. Given that nitrogen typically exhibits a lower collisional deactivation efficiency than propane itself, the relaxation time in the mixture is expected to exceed the self-relaxation time[36]. Consequently, we estimate τ_{VT} to fall within a broad range of 10 ns to 10 μs. For the initial analysis, we provisionally assume τ_{VT}=10 μs to compare the photoacoustic responses under pulsed and modulated-CW excitations. A comprehensive simulation covering the entire range of potential relaxation times is subsequently presented in Fig. 2. Figure 1(b) presents the heat source responses for a Gaussian pulse with full width at half maximum (FWHM) of 2.3 μs and a 50% duty-cycle square wave with equivalent pulse energy. For the 2.3 μs Gaussian pulse, target gas molecules are excited rapidly, after which the heat source exhibits a sharp rise followed by exponential decay as excited molecules gradually release energy through collisional deactivation. In contrast, for the 50% duty-cycle square wave, the generation and decay rates balance during the pulse, maintaining constant excited-state population and thus stable heat source intensity. Figure 1(c) illustrates the transient acoustic pressure responses induced by both pulse types in the resonant PA cell. Both signals experience growth and reach steady state after approximately 5 ms ($\tau=Q/f_0$=4.98 ms, where Q=20.4 and f_0=4100 Hz is the quality factor and the resonance frequency of the PA cell, respectively). Figure 1(d) shows the steady-state responses, where the Gaussian pulse induces significantly enhanced pressure amplitude compared to the square wave. Figure 1(e) shows the Fourier transform of the steady-state pressure signals, indicating that the fundamental frequency component of the low duty cycle Gaussian pulse is about 1.569 times larger than that of the modulated square wave, close to π/2. This enhancement arises from the Fourier characteristics of the corresponding heat source profiles: the LDCP-induced heat source features a rapid rise followed by either exponential decay or the pulse shape itself, as shown in Fig. 2(a) and 2(b). It is important to note that this enhancement stems not from the Gaussian profile but from the low duty-cycle characteristic. As shown in Fig. 2(c), Gaussian and square pulses with identical duty cycles and pulse energy produce nearly identical PA responses, both achieving ~π/2 enhancement over 50%

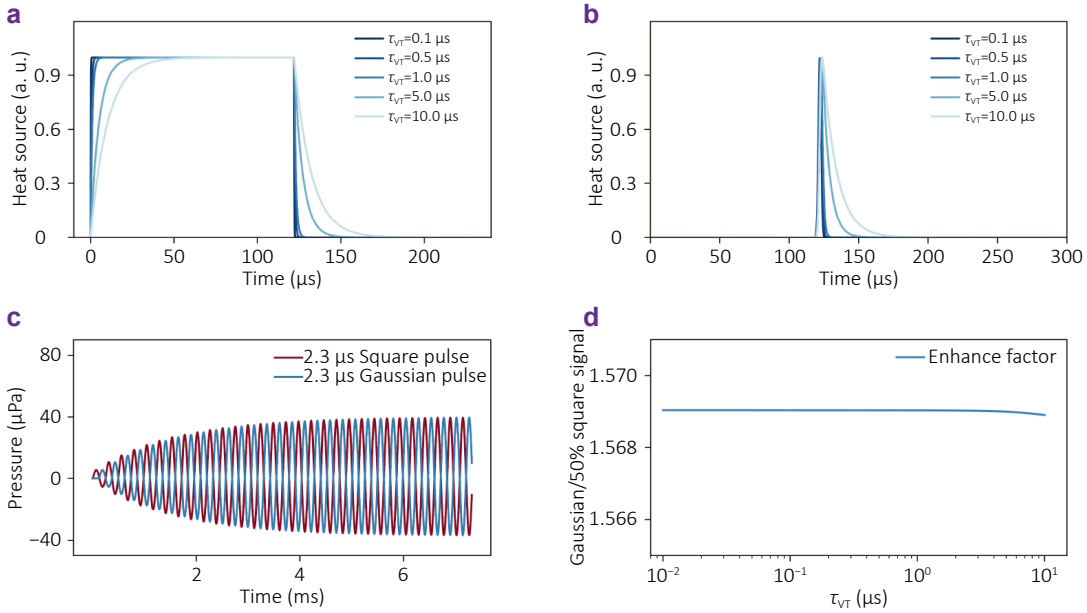

Fig. 2 | Theoretical validation of PA enhancement from LDCP excitation. (a) Simulated temporal profiles of the heat source of 50% duty-cycle square wave pulse and of (b) 2.3 μs Gaussian pulse. (c) Comparison of transient PA pressure signals for a 2.3 μs Gaussian pulse and a 2.3 μs square pulse. (d) The ratio of the PA signal from the LDCP Gaussian pulse to that from a 50% duty-cycle square wave under different V-T relaxation time.

duty-cycle square waves. Figure 1(f) demonstrates the effect of square-wave modulation duty cycle on the PA signal, showing both simulation data and experimental measurements. The experimental method and detailed setup are shown in Supplementary Section 2 and Fig. S2. PA signals were acquired at different AOM duty cycles, and the experimental data were obtained by calculating the PA excitation efficiency η. The results demonstrated that the PA efficiency decreases monotonically with increasing duty cycle, dropping from approximately 1.7-fold at 5% duty cycle to about 0.8-fold at 60% duty cycle (normalized to 50% duty cycle modulated-CW). This trend shows excellent agreement between simulation and experiment, validating the accuracy of the theoretical model. The combination of simulation and experiment effectively confirms the effectiveness of MPEPAS. Furthermore, to validate the robustness of this conclusion, we investigated the PA response across the entire plausible V-T relaxation time range for propane (10 ns to 10 μs). As shown in Fig. 2(d), the signal enhancement factor of LDCP excitation over a 50% duty-cycle square wave remains remarkably stable at approximately 1.569 throughout the potential propane τ_{VT} range of 0.01–10 μs, in close agreement with the theoretical value of π/2.

2.2 Ideal PA excitation platform—GS-MIR fiber laser

The schematic of the GS-MIR fiber laser-based PAS detection is shown in Fig. 3. The system employs 660 nm LDs as the pump source, which is modulated to achieve GS pulsed operation. The pump light passes through a dichroic mirror (DM) and is focused by a coupling lens (L1) into a double-clad Er^{3+}/Dy^{3+} co-doped ZrF_4 fiber. The laser cavity is formed between a front mirror (FM) at the input end and a ruled reflective diffraction grating (RRDG) in Littrow configuration at the rear end, where the first-order diffraction provides feedback for wavelength selection. In this laser system, the long-lived $^4I_{11/2}$ and $^4I_{13/2}$ states of Er^{3+} ions are rapidly depopulated by energy transfer to the codoped Dy^{3+} ions and energy transfer upconversion between the Er^{3+} ions, resulting in the accelerated recycling of ions, which effectively support the high-power output and wide wavelength tunability, and without the need of dual-wavelength pumping[37]. As a result, the high-power tunable GS MIR pulses can be generated. The detailed principle of the Er^{3+}/Dy^{3+} laser is described in Supplementary Section 3, Method section, and our previous work[38]. The output MIR pulses are backward through the DM and directed by a mirror (M1) toward the PAS system. The laser beam diameter is reduced to 0.8 mm by lenses pair L2 and L3, and then directed into a homemade PA cell, of which the resonant frequency is 4100 Hz.

Firstly, we characterized the laser output power at different wavelengths. Under pumping conditions of 50% duty cycle, 4.1 kHz repetition rate, and 22.5 W average power, the wavelength-dependent output power is shown in Fig. 4(a). The laser achieves maximum output power of 245 mW around 3420 nm, benefiting from the high gain of Er^{3+}/Dy^{3+} co-doped fiber in this spectral region. Throughout the 3300–3500 nm range, the output power exceeds 80 mW, fully covering the C–H stretching vibration fingerprint

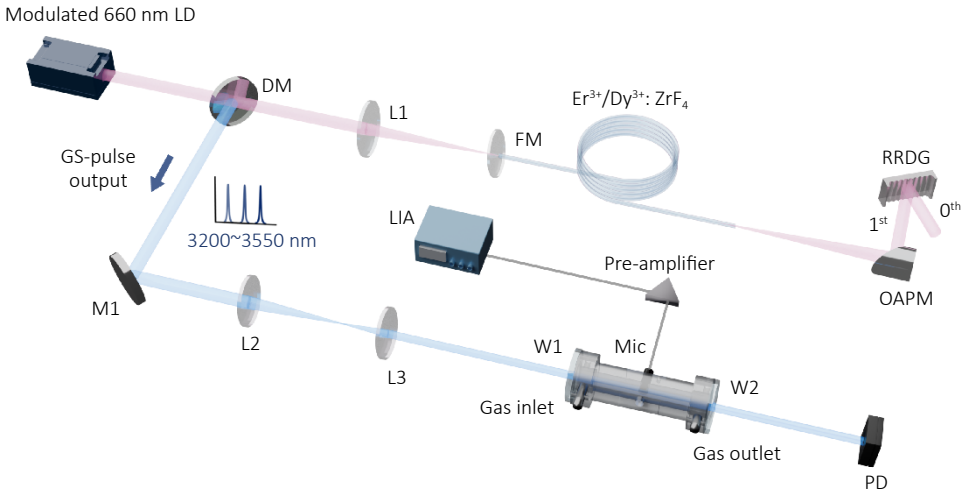

Fig. 3 | GS-MIR Er^{3+}/Dy^{3+} co-doped fiber laser-based PAS detection system. LD: laser diode; DM: dichroic mirror; L1, L2, L3: lenses; FM: front mirror; OAPM: off-axis parabolic mirror; RRDG: ruled reflective diffraction grating; M1: mirror; W1, W2: CaF_2 windows; Mic: microphone; LIA: lock-in amplifier; PD: photodetector.

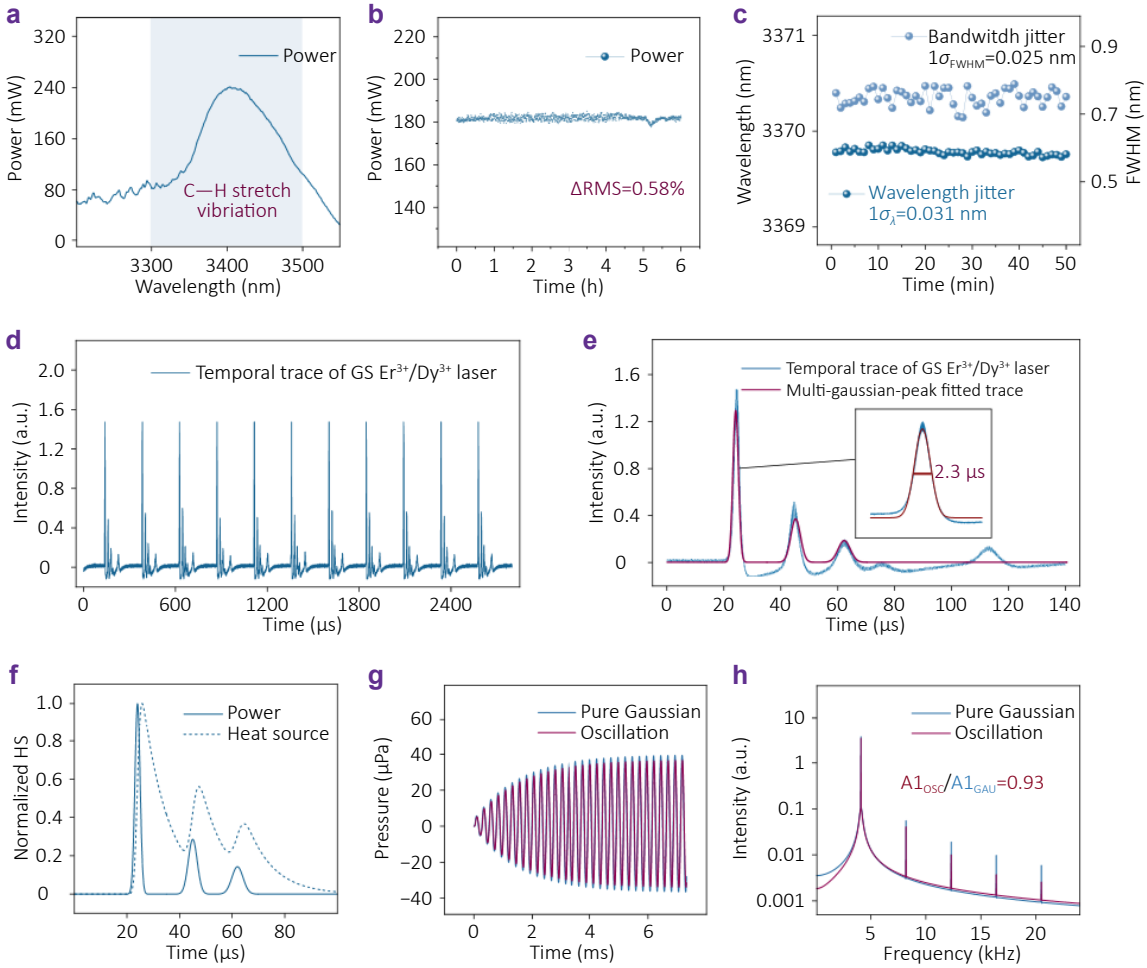

Fig. 4 | Characteristics of the GS-MIR PA excitation source. (a) Output power at different wavelength. (b) Output power stability over 6 hour. (c) Wavelength and bandwidth stability. (d) Experimental measured temporal trace of the GS Er^{3+}/Dy^{3+} laser pulses at a 4.1 kHz repetition rate. (e) Single pulse with relaxation oscillations (temporal trace) and its fitting with a multi-Gaussian function. (f) Heat source of the oscillatory (multi-Gaussian-peak fitted). (g) Comparison of the acoustic pressure driven by pure Gaussian pulse and oscillation pulse. (h) Fourier spectra of the acoustic pressure generated by the oscillatory and Gaussian pulses.

region around 2920 cm^{-1}. The laser repetition rate can be precisely tuned from 1 kHz to 10 kHz by modulating the pump, with the upper limit constrained by the maximum modulation frequency of our LD driver, while the lower limit is primarily determined by increased spontaneous emission losses and insufficient gain recovery at longer pulse intervals, which increases the damage risk of the fiber. For PAS gas detection, power and wavelength stability are crucial parameters, as the PA response is linearly dependent on laser power and strongly correlated with wavelength through the absorption cross-section. Figure 4(b) presents the power stability test results, demonstrating excellent stability with a root-mean-square (RMS) fluctuation of 0.58% over a 6 hours continuous operation period. Wavelength stability was simultaneously monitored at approximately 1 minute sampling intervals, as shown in Fig. 4(c). During the 50 minutes test period, the maximum wavelength drift remained below 0.1 nm, with a standard deviation (1σ) of wavelength jitters of only 0.031 nm. The spectral 3-dB bandwidth also exhibits small jitters of 0.025 nm. This exceptional spectral stability is primarily attributed to the precise wavelength-selective feedback mechanism provided by the RRDG. For the broad absorption features typically exhibited by VOCs, this level of wavelength stability fully satisfies the requirements for high-precision and stable detection.

Figure 4(d) and 4(e) present the temporal characteristics of the laser, revealing a pulse width (FWHM) of approximately 2.3 μs. The pulse exhibits pronounced relaxation oscillations in the trailing edge, which is a characteristic feature of GS pulses arising from the dynamic interplay between the upper-state population and intracavity photon density following abrupt pump termination. The measured pulse property of the GS laser deviates from the idealized Gaussian profile assumed in the theoretical model for comparison with modulated-CW excitation. To accurately reveal how these pulse oscillations affect the PA response, we systematically investigated their influence. A multi-Gaussian pulse model was constructed by fitting the first three high-intensity peaks of the oscillatory pulse, as shown in Fig. 4(e). This was compared with a pure Gaussian pulse (pulse width 2.3 μs) of equivalent pulse energy. The results demonstrate distinct differences in the thermal source effects between the two pulse types, as illustrated in Fig. 4(f) (compared to Fig. 1(d)). However, the acoustics pressure response and the Fourier analysis reveal that the fundamental frequency Fourier coefficients of the oscillatory pulse and Gaussian pulses with identical pulse energy show no significant difference ($A1_{OSC}/A1_{GAU}\approx0.93$), as shown in Fig. 4(g) and 4(h). The substantial differences only appear in the high-frequency harmonic components. Consequently, the oscillatory pulse can still achieve approximately 1.5-fold PA signal enhancement ($\pi/2\times0.93$), demonstrating that the relaxation oscillations do not significantly compromise the enhancement effect predicted by the theoretical model.

This laser employs an elegantly simple architecture, using 660 nm LD pump to produce MIR pulses with tunable temporal characteristics. This design obviates the need for the complex dual-wavelength pumping schemes of conventional systems and any active or passive *Q*-switching components, resulting in a compact, robust, and cost-effective MIR PA excitation source. Furthermore, the GS technique affords precise control over the pulse repetition rate, perfectly matching the frequency requirements for resonant PA detection. Crucially, the laser's low-duty-cycle (0.94%) fully leverage the near-π/2 enhancement factor of MPEPAS. This capability, combined with broad tunability, establishes the laser as an ideal source for the ultrasensitive detection of trace VOCs.

2.3 Ultrasensitive PAS detection of multi-species VOCs

The VOC PA detection system is illustrated in Fig. 3. An electronic pre-amplifier was used to amplify the signals collected by the microphone. All subsequent PA detection experiments were conducted at room temperature and atmospheric pressure, with the lock-in amplifier time constant set to 100 ms. The test gas concentration was controlled using mass flow controllers, and measurements were performed at a fixed flow rate of 200 mL/min to meet the requirements for real-time sampling and monitoring in industrial/environmental applications. The dimensions of the custom-designed resonant PA cell were shown in Supplementary Section 4.

Propane, a typical broadband-absorbing alkane VOC, was first selected as the target gas for measurement. The absorption spectrum of propane, obtained from the HITRAN database, is shown in Fig. 5(h). The peak absorption occurs around 3369 nm; therefore, the wavelength was fixed at 3369 nm by tuning the RRDG, yielding a laser output power of ~180 mW. The variation of propane PA signal with concentration is shown in Fig. 5(a) and 5(b), demonstrating excellent linear response to propane concentration with $R^2>0.999$. For comparison, we constructed a PA detection system based on AOM-modulated CW laser, of which the system is shown in Supplementary Section 2. Compared to the GS-PAS system, this configuration utilized a CW pumping and adding an AOM between the PA cell and output laser for frequency modulation. By controlling the pump power, the modulated CW power transmitted through the PA cell was adjusted to 60 mW. The PA response at 100 ppm concentration is shown in Fig. 5(c). Additionally, we reduced the GS laser power so that the transmitted power through the PA cell was also 60 mW. The results show that, compared to the modulated CW laser, the GS laser enhanced the PA response by 1.96-fold at the same average power, supported by the theoretical π/2 MPEPAS enhancement factor. The additional enhancement may result from model errors, as our theoretical model did not account for thermal diffusion

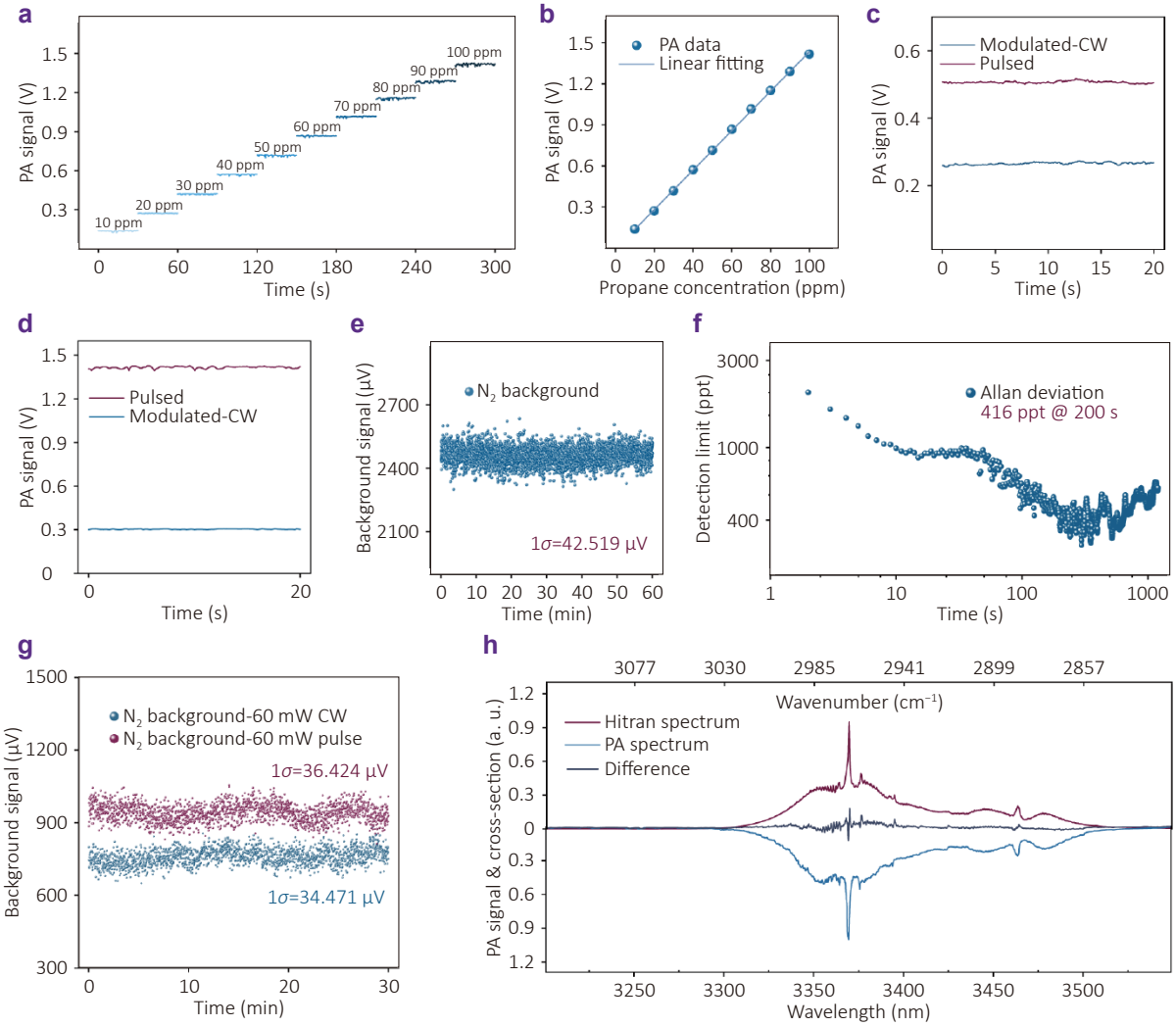

Fig. 5 | Propane detection performance and spectroscopic characterization of the GS-PAS system. (a) PA signals at different propane concentrations from 10 to 100 ppm. (b) Linear fitting curve of PA signal versus propane concentration. (c) Comparison of PA signals between modulated CW laser (blue) and pulsed GS laser (red) at 60 mW average power for 100 ppm propane. (d) PA signal comparison between pulsed and modulated CW systems under identical 22.5 W pump power conditions. (e) N_2 background noise. (f) Allan deviation analysis demonstrating a detection limit of 416 ppt at 200 s integration time. (g) Background noise comparison between 60 mW CW (blue) and pulsed (red) laser configurations. (h) PA spectrum of propane in the 3200–3550 nm range (blue) compared with HITRAN database reference spectrum (red).

processes, which involve multiple factors including gas thermal relaxation and collisions with the PA cell walls, making quantitative analysis challenging. Nevertheless, both theoretical and experimental results effectively demonstrate the MPEPAS effect. Furthermore, we measured the PA response of both laser configurations under identical pump power conditions of 22.5 W. The results, shown in Fig. 5(d), reveal that the GS system achieved a 4-fold improvement in PA signal compared to the modulated CW system under the same pump conditions, further confirming the high energy utilization efficiency of the pulsed PA laser system.

We also characterized the background noise level of the GS-PAS system by introducing pure nitrogen at the same flow rate. As shown in Fig. 5(e), at 180 mW power, the system exhibited a background of approximately 2.45 mV, yielding a signal-to-background ratio (SBR) of 580 for 100 ppm propane. This background primarily originates from absorption by the CaF_2 windows. Under identical experimental conditions, sapphire windows produced a higher background of approximately 9 mV, the larger sapphire-induced background shown in Supplementary Fig. S6(a) confirming the significant impact of window materials on SBR. Therefore, employing thinner windows would effectively improve the SBR. For CaF_2 windows, the measured 1σ noise was 42.5 μV, resulting in a signal-to-noise ratio exceeding 33435 for 100 ppm propane concentration with 100 ms integration time, corresponding to a detection limit of 2.99 ppb. Finally, we evaluated the long-term stability of

the system, as shown in Fig. 5(f). Combined with Allan deviation analysis, a detection limit of 416 ppt for propane was achieved with a 200 s integration time, representing an improvement of more than an order of magnitude over state-of-the-art PAS systems, as detailed in Table 1. The low power-normalized noise equivalent absorption (NNEA, $NNEA=\frac{P\alpha_{\min}}{\sqrt{BW}}$) of 2.16×10^{-8} W·cm^{-1}·Hz$^{-1/2}$, calculated using the average power P, minimum detectable absorption coefficient $\alpha_{\min}$, and the equivalent bandwidth of the lock-in amplifier, indicates that the achieved detection limit stems not only from the high average power of the GS MIR laser but also from the signal enhancement induced by microsecond pulses, the high power utilization efficiency, the suppression of wall noise enabled by the fiber laser's high beam quality, and the elimination of mechanical noise via GS modulation. The noise levels of the modulated CW system were also measured for comparison, as shown in Fig. 5(g). In this comparison, both configurations operated at the same power of 60 mW. The results indicate that both configurations exhibit similar noise levels at the same average power, demonstrating that the pulsed laser enhances PA response without introducing additional noise, effectively improving the signal-to-noise ratio by nearly a factor of two. This confirms the effectiveness of pulsed lasers in improving detection limits.

Utilizing the broadband tuning capability of our laser, we obtained the PA spectrum of propane in the C–H fingerprint region from 3200–3550 nm by controlling the grating rotation angle, as shown in Fig. 5(h). This effectively characterizes the absorption properties of propane. Theoretically, the PA spectral resolution is primarily determined by the laser's FWHM bandwidth of < 0.8 nm (shown in Fig. S3(e–g) of Supplementary Section 3), which is sufficient to reconstruct the infrared spectrum of propane. The discrepancy observed near 3369 nm is attributed to the mismatch between the FWHM of this sharp absorption peak (0.62 nm) and the laser bandwidth (0.7 nm), resulting in reduced spectral power density utilization efficiency. Nevertheless, the obtained results show excellent consistency with HITRAN database data, which highlights the great potential of the broadband tunable GS fiber laser for acquiring full absorption spectra, enabling simultaneous detection of multiple gas species through the deconvolution of overlapped PA spectra. Furthermore, we systematically evaluated the detection performance for three representative VOCs, 1,2-Dimethoxyethane, Propanal, and Isoprene (absorption cross-sections are plotted in Supplementary Fig. S7), to demonstrate the versatility of our system. Detection was performed by targeting their characteristic C–H absorption bands at 3342 nm, 3465 nm, and 3382 nm, respectively. As shown in Fig. 6, all gases exhibit excellent linear PA response with correlation coefficients exceeding 0.999. With a lock-in time constant of 100 ms, detection limits of 19.1 ppb, 7.4 ppb, and 20.1 ppb were achieved for propanal, 1,2-dimethoxyethane, and isoprene, respectively. By extending the averaging time to 200 s, the limits of detection were further improved to 1.8 ppb, 0.85 ppb, and 2.67 ppb, respectively, representing state-of-the-art performance in photoacoustic VOC detection.

3 Discussion

The high-power and widely tunable GS MIR fiber laser system brings significant improvements to PA detection. The system effectively simplifies the PA detection setup compared to modulated-CW approaches, while achieving enhanced PA response by MPEPAS and high energy utilization efficiency, effectively reducing the detection limit. Through theoretical modeling, we have elucidated the origin of this enhancement. Unlike ref.[32], which only compared ultrashort pulses (picosecond to nanosecond) with modulated CW cases, we have investigated the PA response induced by pulsed lasers on timescales comparable to τ_{VT}, filling the gap in this temporal regime. Notably, microsecond-scale pulses are particularly well-suited for PAS detection, as their repetition rates typically range from few-kHz to hundreds of kHz, which coincides with the typical resonance frequencies of acoustic resonators.

It should be noted that we are by no means the first to employ pulsed lasers for PA trace gas detection. Many literature have demonstrated PA detection using pulsed lasers

Table 1 | Comparison of state-of-the-art PAS propane detection performance.

Laser	Wavelength (μm)	Power (mW)	Modulated method	Averaging time (s)	Detection limit (ppb)	NNEA (W·cm^{-1}·Hz$^{-1/2}$)	Ref.
DFB	1.654	N/A	N/A	0.001	40260	N/A	ref.[39]
OPO	3.369	1200	Chopper	1	13.2	8.84×10^{-7}	ref.[40]
QCL	13.36	3	2*f*-WMS	10	3000	2.82×10^{-8}	ref.[10]
ICL	3.349	N/A	2*f*-WMS	N/A	3000	N/A	ref.[41]
ICL	3.382	N/A	Chopper	20	64	N/A	ref.[30]
ICL	3.349	11	2*f*-WMS	1	3000	6.55×10^{-7}	ref.[42]
ICL	3.368	10	2*f*-WMS	20	419	5.11×10^{-7}	ref.[43]
GS-MIR fiber laser	**3.369**	**180**	**Pulse-enhanced**	**1 & 200**	**2.15 & 0.416**	**2.16×10^{-8}**	**This work**

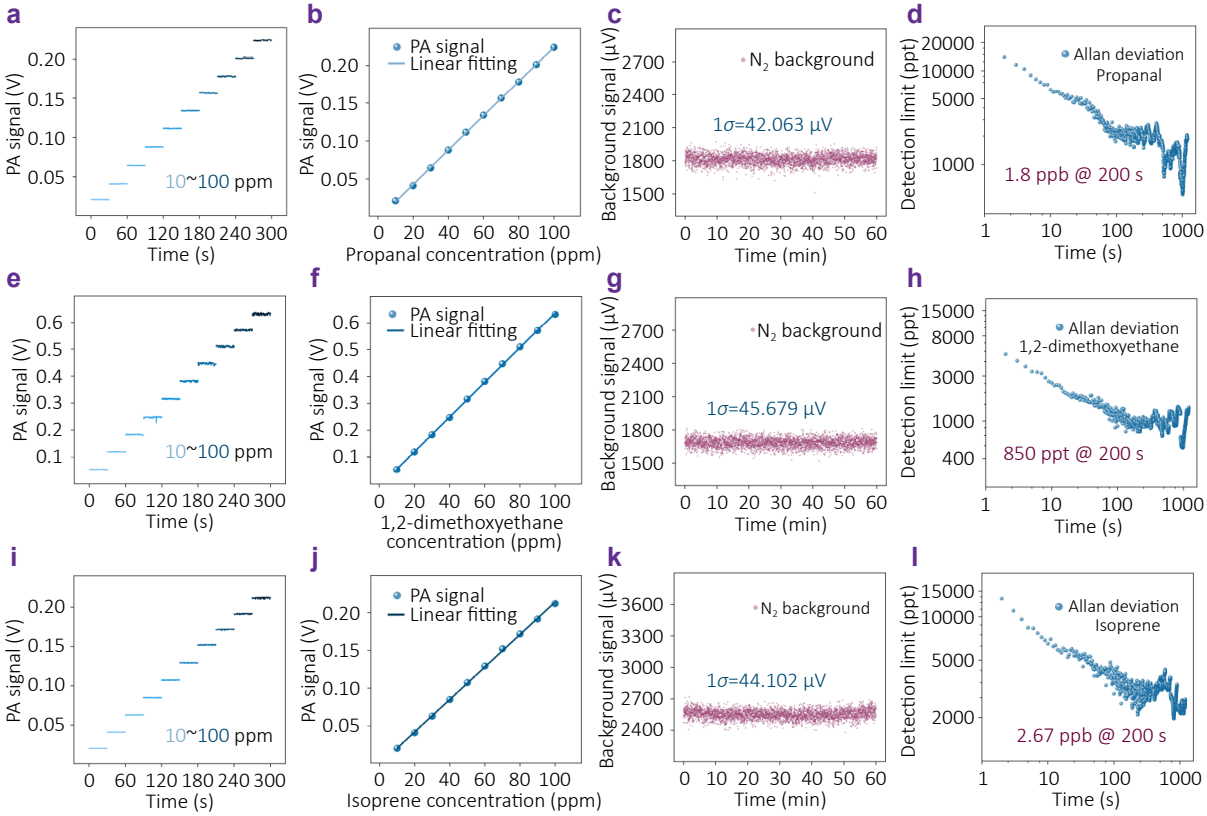

Fig. 6 | PA measurement results for propanal (a–d), 1,2-dimethoxyethane (e–h), and isoprene (i–l). First row (a, e, i): step response of PA signals for gas concentrations from 10 to 100 ppm with 10 ppm increments. Second row (b, f, j): linear fitting curve of PA signal versus different concentration. Third row (c, g, k): background noise measurements in pure N_2 over 60 minutes. Fourth row (d, h, l): Allan deviation analysis showing minimum detection limits of 1.8 ppb (propanal), 850 ppt (1,2-dimethoxyethane), and 2.67 ppb (isoprene) at 200 s integration time.

including CO_2 lasers, OPO, and solid laser[44–49], although the authors did not elaborate on the enhancement effect of pulsed lasers. In this study, because the operating mode of the Er^{3+}/Dy^{3+} laser can be readily switched between CW and pulsed regimes simply by altering the pumping scheme (rather than using two separate lasers), we are able to rigorously validate this enhancement. Interestingly, PA imaging has almost exclusively adopted pulsed lasers to achieve high spatial resolution and deep tissue penetration through the generation of strong, transient PA signals[50–52]. In contrast, CW lasers have remained the absolute mainstream in PA gas detection. Such a significant disparity within the same technique is particularly intriguing. This phenomenon can be attributed to the easy accessibility of CW lasers (e.g., DFB, ICL, or QCL sources), the longstanding neglect of the pulse-enhanced effect in PAS, and most importantly, the fact that conventional pulsed lasers inherently operate at repetition rates mismatched with the acoustic resonator frequency, thus requiring additional modulation components that obscure their intrinsic advantages. The GS-MIR fiber laser-based MPEPAS perfectly addresses these issues, effectively unlocking the enormous potential of pulse-enhanced photoacoustic effects.

Compared to OPO-based PA systems, GS fiber lasers offer simpler system architecture, superior beam quality, and enhanced stability. Furthermore, unlike the high-repetition-rate OPO schemes reported in previous works[23,40,53], GS fiber lasers can directly match acoustic resonance frequencies, substantially improving power utilization efficiency. Compared to 1 W OPO-based propane detection[40], despite the lower power of the GS-MIR laser, we still achieved further reduction in detection limits from 13.2 ppb to 2.15 ppb (1 s LIA time constant, noise property shows in Supplementary Fig. S6(b)), benefiting from the pulse-enhanced effect, high power utilization efficiency, and suppressed wall noise and mechanical noise resulting from the superior beam quality and GS modulation. Relative to ICL-based PA detection, the high-power capability of the GS-MIR fiber laser effectively advances propane detection limits from ppm/ppb of ref.[20,30,42,43] to ppt levels. While QCL detection schemes target VOC resonances at longer wavelengths (e.g., C=O bonds, aromatic C–H stretches) to achieve ultralow detection limits[10,54], our system operating in the C–H fingerprint region holds the potential for competitive

performance by leveraging the high power and pulse-enhanced properties of this laser. Moreover, the single-wavelength output or narrow tuning range of individual QCL chips limits their multi-gas detection capability, whereas combining multiple QCLs or employing external-cavity QCLs significantly increases system cost. Admittedly, the current hybrid fiber-spatial architecture limits the system's compactness compared to highly integrated DFB or QCL-based solutions. However, with the increasing maturation of mid-infrared fiber components, such as combiners, isolators, and fiber Bragg gratings, the future transition to a fully all-fiber architecture will drive further miniaturization, ultimately enabling truly portable operation.

The broadband absorption of VOCs renders traditional 2*f*-WMS ineffective. In ref.[10,20,41,42], the authors employed the same WMS system to detect methane, ethane, and propane, they achieved ppb-level detection for methane and ethane but were limited to ppm-level detection for propane, primarily because the wavelength modulation depth (typically < 1 nm) is far smaller than propane's absorption bandwidth. Consequently, intensity modulation emerges as the optimal approach for VOC detection. GS pulsed fiber lasers not only eliminate the additional insertion losses (≥3 dB) and system complexity associated with AOMs or mechanical choppers but, more importantly, their pulsed characteristics enable significant PA enhancement. As a consequence, GS MIR fiber lasers demonstrate tremendous advantages for VOCs PA detection.

Despite these significant achievements, opportunities for further improvement remain. Regarding theoretical modeling, the current model primarily addresses heat source and acoustic pressure generation without considering heat diffusion and equilibration processes, resulting in discrepancy between the theoretically predicted pulse enhancement factor (1.57-fold) and experimental observation (1.96-fold). Future work incorporating heat diffusion equations with appropriate boundary conditions could more accurately describe the complete PA generation process.

For practical applications, water vapor interference represents a critical challenge. While our experimental setup effectively prevented environmental moisture penetration through excellent chamber sealing and constant-flow gas mixing, percentage-level water content is unavoidable in real environmental monitoring and breath analysis applications. Two mitigation strategies can be employed: first, exploiting the spectral differences between VOC's broadband absorption and water's sparse absorption to precisely select wavelengths where water absorption is relatively weak (as shown in Supplementary Fig. S8); second, integrating molecular sieves in the gas inlet for physical dehumidification. For ultra-high precision applications such as biomedical VOC detection, simultaneous implementation of both methods is recommended. To further reduce the detection limit, using a higher-sensitivity microphone to increase the signal and an anti-reflection coated thinner ZnSe window to reduce absorption background are effective methods to improve the SNR. Moreover, a high-frequency modulating LD driver can be employed at the resonant frequency of quartz tuning forks (~33 kHz). By integrating GS technology with both quartz-enhanced PA spectroscopy (QEPAS) and cavity-enhanced PA spectroscopy[55], and leveraging the superior beam quality and power characteristics of fiber lasers, propane detection limits could potentially be advanced to few-ppt or even sub-ppt levels. Finally, employing methods such as etalons, volume Bragg gratings, and optical feedback frequency stabilization to achieve narrow linewidth pulsed laser output will unleash the potential of the GS laser based MPEPAS in absorption spectrum construction[56]. Combing with machine learning algorithms (e.g., principal component analysis, neural networks) for mixed VOCs spectral deconvolution[57], will further unlock this system's tremendous potential in biomedical diagnostics, environmental monitoring, industrial process control, and related applications.

4 Conclusions

In this work, we developed and experimentally validated the first VOC photoacoustic detection system based on a mid-infrared fiber laser, introducing MPEPAS as a new detection paradigm. By precisely matching the microsecond pulse duration and repetition rate with the acoustic resonance frequency, the system achieved nearly two-fold enhancement in photoacoustic response compared to conventional continuous-wave modulation under identical power, fundamentally revealing the previously overlooked advantage of pulsed excitation in the microsecond regime. The GS-MIR fiber laser provides high peak power, broad tunability across the 3.2–3.55 μm C–H absorption region, and excellent beam quality within a simple, compact design, enabling record-breaking sensitivity—achieving a 416 ppt detection limit for propane and ppb-level sensitivity for other VOCs such as propanal, isoprene, and 1,2-dimethoxyethane. Compared to OPO, QCL, and ICL based systems, this approach delivers comparable or superior sensitivity with lower cost, higher stability, and simpler configuration by eliminating external modulators and maximizing power utilization efficiency. These results not only demonstrate the potential of GS fiber lasers as high-performance MIR sources but also mark a shift in photoacoustic spectroscopy from conventional CW-driven schemes to resonance-synchronized pulsed excitation. With further integration into quartz- or cavity-enhanced configurations, and through the incorporation of narrow-linewidth pulse control and intelligent spectral analysis techniques, this method could push VOC detection into the sub-ppt regime and enable precise multi-species analysis. Overall, the proposed GS-MIR laser-based MPEPAS establishes a new benchmark for ultrasensitive and practical photoacoustic VOC detection, offering transformative potential for biomedical diagnostics, environmental monitoring, and industrial safety applications.

5 Materials and methods

5.1 Er^{3+}/Dy^{3+} GS fiber laser setup

In the GS laser setup, the commercial 660 nm LDs (Huaguang optoelectronics) served as the optical pump source. The LD was powered by a custom-designed modulation driver capable of duty cycle adjustment from 10% to 50% and current modulation frequencies up to 10 kHz. The active medium consisted of a double-clad Er^{3+}/Dy^{3+} co-doped fluoride fiber (fiberlabs) with a length of 4.2 m length and dopant concentrations of 4/0.25 mol.% for Er^{3+}/Dy^{3+}, respectively. The fiber core featured a diameter of 17.3 μm with numerical aperture of 0.13, while the circular inner cladding with diameter of 249 μm and NA of 0.5. Thermal management was implemented through water-cooled clamps maintaining 18 °C at both 9 cm terminal sections, with the fiber body positioned on a passive aluminum heat sink. The pump-end fiber facet received perpendicular cleaving and direct coupling to a front mirror exhibiting high transmission at 660 nm and reflectivity at 2.7–3.7 μm (0° incidence) for cavity feedback. The output end incorporated an 8° angle-cleave to suppress parasitic oscillations, with no protective end caps employed. Wavelength-selective feedback was achieved using a ruled reflective diffraction grating (Thorlabs, GR2550-30035) mounted on a precision rotational stage (JCOPTIX, DORR-360HK). Output characterization employed thermal power sensors (Thorlabs, S405C) for power measurements, while temporal pulse profiles were captured using an HgCdTe detector (VIGO, PCI-2TE-12) coupled to a 500 MHz digital oscilloscope. Spectral analysis utilized a high-resolution optical spectrum analyzer (Yokogawa, AQ6377).

5.2 PA detection of trace VOCs

In the PAS system, a resonant PA cell (detailed in Supplementary Section 4) was employed to amplify the PA signal. The acoustic signal was collected using an electret condenser microphone (Primo, EM258), with the electrical output transmitted via shielded audio cable (Canare, L-2B2AT). A custom electronic amplifier (Hongchuang Electronics) provided adjustable electrical signal amplification ranging up to 50×, notably, all the measurements were conducted using the maximum electrical amplification. Lock-in detection was implemented using a compact lock-in amplifier board (Yishi Electronics, YHLAI1620) with a footprint of approximately 12 cm×10 cm, featuring integrated reference clock and analog-to-digital conversion, eliminating the need for external reference signals and additional data acquisition hardware. Precise gas mixing and constant flow rates were achieved using a custom gas handling system (Aurasky, CS-41).

References

1. World Health Organization. WHO global air quality guidelines: particulate matter ($PM_{2.5}$ and PM_{10}), ozone, nitrogen dioxide, sulfur dioxide and carbon monoxide. (World Health Organization, 2021).
2. Rooth G, Östenson S. Acetone in alveolar air, and the control of diabetes. *Lancet* **288**, 1102–1105 (1966).
3. Curtius J, Heinritzi M, Beck LJ et al. Isoprene nitrates drive new particle formation in Amazon's upper troposphere. *Nature* **636**, 124–130 (2024).
4. Li L, Zhang D, Hu W et al. Improving VOC control strategies in industrial parks based on emission behavior, environmental effects, and health risks: a case study through atmospheric measurement and emission inventory. *Sci Total Environ* **865**, 161235 (2023).
5. Davoli E, Gangai ML, Morselli L et al. Characterisation of odorants emissions from landfills by SPME and GC/MS. *Chemosphere* **51**, 357–368 (2003).
6. Ycas G, Giorgetta FR, Cossel KC et al. Mid-infrared dual-comb spectroscopy of volatile organic compounds across long open-air paths. *Optica* **6**, 165–168 (2019).
7. Liang QZ, Bisht A, Scheck A et al. Modulated ringdown comb interferometry for sensing of highly complex gases. *Nature* **638**, 941–948 (2025).
8. Choi YM, Cho SY, Jang D et al. Ultrasensitive detection of VOCs using a high-resolution CuO/Cu_2O/Ag nanopattern sensor. *Adv Funct Mater* **29**, 1808319 (2019).
9. Cho SY, Yoo HW, Kim JY et al. High-resolution p-type metal oxide semiconductor nanowire array as an ultrasensitive sensor for volatile organic compounds. *Nano Lett* **16**, 4508–4515 (2016).
10. Kinjalk K, Paciolla F, Sun B et al. Highly selective and sensitive detection of volatile organic compounds using long wavelength InAs-based quantum cascade lasers through quartz-enhanced photoacoustic spectroscopy. *Appl Phys Rev* **11**, 021427 (2024).
11. Qiao SD, He Y, Sun HY et al. Ultra-highly sensitive dual gases detection based on photoacoustic spectroscopy by exploiting a long-wave, high-power, wide-tunable, single-longitudinal-mode solid-state laser. *Light Sci Appl* **13**, 100 (2024).
12. Mu JJ, Han GW, Wang RQ et al. Photoacoustic spectroscopy and light-induced thermoelastic spectroscopy based on inverted-triangular lithium niobate tuning fork. *Opto-Electron Sci* **4**, 250035 (2025).
13. Qiao SD, Liu XN, Lang ZT et al. Quartz-enhanced laser spectroscopy sensing. *Light Sci Appl* **15**, 5 (2026).
14. Wang RQ, Qiao SD, He Y et al. Highly sensitive laser spectroscopy sensing based on a novel four-prong quartz tuning fork. *Opto-Electron Adv* **8**, 240275 (2025).
15. Ma J, Fan EB, Liu HJ et al. Microscale fiber photoacoustic spectroscopy for in situ and real-time trace gas sensing. *Adv Photonics* **6**, 066008 (2024).
16. Wang H, Xu YF, Zhang JY et al. Fiber-optic photoacoustic gas microprobe based on linear spot-type multipass cell. *Anal Chem* **97**, 1300–1308 (2025).
17. Cui RY, Yuan YP, Qui S et al. Miniaturized 3D-printed multipass helmholtz photoacoustic sensors for high-sensitivity CO_2 detection with near-infrared (NIR) diode lasers. *Anal Chem* **97**, 13095–13102 (2025).
18. Faist J, Capasso F, Sivco DL et al. Quantum cascade laser. *Science* **264**, 553–556 (1994).
19. Ma YF, Lewicki R, Razeghi M et al. QEPAS based ppb-level detection of CO and N_2O using a high power CW DFB-QCL. *Opt Express* **21**, 1008–1019 (2013).
20. Cantatore AFP, Menduni G, Zifarelli A et al. Methane, ethane, and propane detection using a quartz-enhanced photoacoustic sensor for natural gas composition analysis. *Energy Fuels* **39**, 638–646 (2025).
21. DeMille S, deLaat RH, Tanner RM et al. Comparison of CRDS to ICL-PAS and phase-shift CRDS spectroscopies for the absolute

intensities of C-H (Δv_{CH}=6) overtone absorptions. *Chem Phys Lett* **366**, 383–389 (2002).
22. Saalberg Y, Wolff M. Multivariate analysis as a tool to identify concentrations from strongly overlapping gas spectra. *Sensors* **18**, 1562 (2018).
23. Saalberg Y, Bruhns H, Wolff M. Photoacoustic spectroscopy for the determination of lung cancer biomarkers-a preliminary investigation. *Sensors* **17**, 210 (2017).
24. Jackson SD. Towards high-power mid-infrared emission from a fibre laser. *Nature Photonics* **6**, 423–431 (2012).
25. Petersen CR, Møller U, Kubat I et al. Mid-infrared supercontinuum covering the 1.4–13.3 μm molecular fingerprint region using ultra-high NA chalcogenide step-index fibre. *Nature Photonics* **8**, 830–834 (2014).
26. Wang YZ, Hong LJ, Zhang CL et al. Synthesizing gas-filled anti-resonant hollow-core fiber Raman lines enables access to the molecular fingerprint region. *Nat Commun* **15**, 9427 (2024).
27. Mikkonen T, Hieta T, Genty G et al. Sensitive multi-species photoacoustic gas detection based on mid-infrared supercontinuum source and miniature multipass cell. *Phys Chem Chem Phys* **24**, 19481–19487 (2022).
28. Seddon AB, Tang ZQ, Furniss D et al. Progress in rare-earth-doped mid-infrared fiber lasers. *Opt Express* **18**, 26704–26719 (2010).
29. Jobin F, Paradis P, Aydin YO et al. Recent developments in lanthanide-doped mid-infrared fluoride fiber lasers [Invited]. *Opt Express* **30**, 8615–8640 (2022).
30. Loh A, Wolff M. Multivariate analysis of photoacoustic spectra for the detection of short-chained hydrocarbon isotopologues. *Molecules* **25**, 2266 (2020).
31. Wei QH, Li BC, Zhao BX et al. EC-QCL based photoacoustic spectroscopy for detection of SF_6 decomposition components. *Sens Actuators B Chem* **369**, 132351 (2022).
32. Bartlome R, Kaučikas M, Sigrist MW. Modulated resonant versus pulsed resonant photoacoustics in trace gas detection. *Appl Phys B* **96**, 561–566 (2009).
33. Sigrist MW, Winefordner JD, Kolthoff IM. *Air Monitoring by Spectroscopic Techniques* (Wiley, New York, 1994).
34. Miklós A, Hess P, Bozóki Z. Application of acoustic resonators in photoacoustic trace gas analysis and metrology. *Rev Sci Instrum* **72**, 1937–1955 (2001).
35. Holmes R, Jones GR, Pusat N. Vibrational relaxation in propane, propylene, and ethane. *J Chem Phys* **41**, 2512–2516 (1964).
36. Müller M, Rück T, Jobst S et al. An algorithmic approach to compute the effect of non-radiative relaxation processes in photoacoustic spectroscopy. *Photoacoustics* **26**, 100371 (2022).
37. Henderson-Sapir O, Munch J, Ottaway DJ. Mid-infrared fiber lasers at and beyond 3.5 μm using dual-wavelength pumping. *Opt Lett* **39**, 493–496 (2014).
38. Luo HY, Wang YZ, Chen JS et al. Red-diode-clad-pumped Er^{3+}/Dy^{3+} codoped ZrF_4 fiber: a promising mid-infrared laser platform. *Opt Lett* **47**, 5313–5316 (2022).
39. Zhuang RB, He JF, Lin HY et al. Conductance-photoacoustic spectroscopy for fast and concurrent sensing of hydrogen and hydrocarbons. *Photoacoustics* **45**, 100752 (2025).
40. Bruhns H, Wolff M, Saalberg Y et al. Quantitative evaluation of broadband photoacoustic spectroscopy in the infrared with an optical parametric oscillator. *Sensors* **18**, 3971 (2018).
41. Luo P, Harrist J, Menduni G et al. Simultaneous detection of methane, ethane, and propane by QEPAS sensors for on-site hydrocarbon characterization and production monitoring. *ACS Omega* **7**, 3395–3406 (2022).
42. Sampaolo A, Csutak S, Patimisco P et al. Methane, ethane and propane detection using a compact quartz enhanced photoacoustic sensor and a single interband cascade laser. *Sensors Actuat B Chem* **282**, 952–960 (2019).
43. Mei HY, Wang GX, Xu YH et al. Simultaneous measurement of methane, propane and isobutane using a compact mid-infrared photoacoustic spectrophone. *Photoacoustics* **39**, 100635 (2024).
44. Lassen M, Lamard L, Feng YY et al. Off-axis quartz-enhanced photoacoustic spectroscopy using a pulsed nanosecond mid-infrared optical parametric oscillator. *Opt Lett* **43**, 5667–5670 (2018).
45. Slezak V, Santiago G, Peuriot AL. Photoacoustic detection of NO_2 traces with CW and pulsed green lasers. *Opt Lasers Eng* **40**, 33–41 (2003).
46. Slezak V. High-precision pulsed photoacoustic spectroscopy in NO_2-N_2. *Appl Phys B* **73**, 751–755 (2001).
47. Pushkarsky MB, Webber ME, Patel CKN. Ultra-sensitive ambient ammonia detection using CO_2-laser-based photoacoustic spectroscopy. *Appl Phys B* **77**, 381–385 (2003).
48. Nidheesh VR, Mohapatra AK, Nayak R et al. UV laser-based photoacoustic breath analysis for the diagnosis of respiratory diseases: detection of asthma. *Sens Actuators B Chem* **370**, 132367 (2022).
49. Zhang QD, Chang J, Cong ZH et al. Pptv-level intra-cavity QEPAS sensor for acetylene detection using a high power Q-switched fiber laser. *IEEE Sensors J* **19**, 6181–6186 (2019).
50. Wang LV. Multiscale photoacoustic microscopy and computed tomography. *Nat Photonics* **3**, 503–509 (2009).
51. Shi JH, Wong TTW, He Y et al. High-resolution, high-contrast mid-infrared imaging of fresh biological samples with ultraviolet-localized photoacoustic microscopy. *Nat Photonics* **13**, 609–615 (2019).
52. Zhu XY, Huang Q, DiSpirito A et al. Real-time whole-brain imaging of hemodynamics and oxygenation at micro-vessel resolution with ultrafast wide-field photoacoustic microscopy. *Light Sci Appl* **11**, 138 (2022).
53. Angstenberger S, Floess M, Schmid L et al. Coherent control in quartz-enhanced photoacoustics: fingerprinting a trace gas at ppm-level within seconds. *Optica* **12**, 1–4 (2025).
54. Pangerl J, Sukul P, Rück T et al. Photoacoustic trace-analysis of breath isoprene and acetone via interband- and Quantum Cascade Lasers. *Sensors Actuat B Chem* **424**, 136886 (2025).
55. Ma YF, Qiao SD, He Y et al. Highly sensitive acetylene detection based on multi-pass retro-reflection-cavity-enhanced photoacoustic spectroscopy and a fiber amplified diode laser. *Opt Express* **27**, 14163–14172 (2019).
56. Saikawa J, Fujii M, Ishizuki H et al. High-energy, narrow-bandwidth periodically poled Mg-doped $LiNbO_3$ optical parametric oscillator with a volume Bragg grating. *Opt Lett* **32**, 2996–2998 (2007).
57. Cao YN, Fu WL, Cheng G et al. High-precision photoacoustic sensor utilizing novel rollar-type photoacoustic resonator and dense convolutional network (DenseNet). *Sensors Actuat B Chem* **444**, 138328 (2025).

Acknowledgements

The authors are grateful for the financial support from the National Natural Science Foundation of China (62575051), Equipment Pre research Joint Fund of the Ministry of Education (8091B042228), Science and Technology Project of Sichuan Province (2023NSFSC1964, 2023NSFSC0033), Stability Support Special Project of the Southwest Institute of Technical Physics (No.2024-WZ-9), Tianfu Jiangxi Laboratory (641419), and the Chinese Scholarship Council.

Author contributions

J. L., B. L., and S. W. proposed the original concept, X. Z., S. W., and H. L. built up the laser, S. W., L. Z., and W. W. built up the photoacoustic detection system. S. W., M. J., and J. W. designed the photoacoustic cell, S. W., L. Z., and H. L. wrote the original manuscript; J. L., X. Z., H. L., and B. Z. revised the paper; J. L., Y. L., and H. L. supervised the study, all authors discussed the results and commented on the manuscript.

Competing interests

The authors declare no competing financial interests.

Data availability

The data that support the study are available upon reasonable request to the corresponding author.

Supplementary information

Supplementary information for this paper is available at
https://doi.org/10.29026/oes.2026.260008